Probing trade-off between critical size and velocity in cold-spray: An atomistic simulation

Mahyar Ghasemi, Alireza Seifi, Movaffaq Kateb, Jón Tómas Gudmundsson, Pascal Brault, Pirooz Marashi

Journal of Vacuum Science and Technology A

RESEARCH ARTICLE | NOVEMBER 05 2024

Probing trade-off between critical size and velocity in cold-pray: An atomistic simulation

Mahyar Ghasemi ; Alireza Seifi ; Movaffaq Kateb ; Jon Tomas Gudmundsson ; Pascal Brault ; Pirooz Marashi

J. Vac. Sci. Technol. A 42, 063108 (2024)
https://doi.org/10.1116/6.0003968

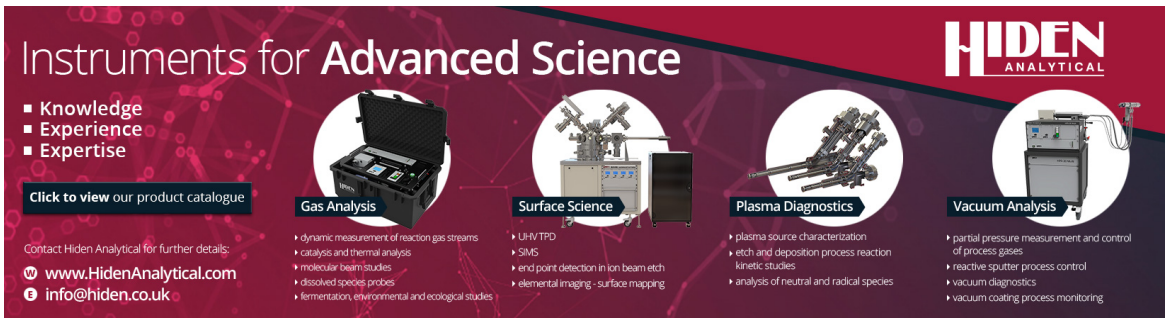

JVST A
Journal of Vacuum Science & Technology A

ARTICLE

pubs.aip.org/avs/jva

Probing trade-off between critical size and velocity in cold-pray: An atomistic simulation

Cite as: J. Vac. Sci. Technol. A 42, 063108 (2024); doi: 10.1116/6.0003968
Submitted: 7 August 2024 · Accepted: 16 October 2024 ·
Published Online: 5 November 2024

Mahyar Ghasemi,[1] Alireza Seifi,[1] Movaffaq Kateb,[2,a)] Jon Tomas Gudmundsson,[3,4] Pascal Brault,[5] and Pirooz Marashi[1]

AFFILIATIONS

[1]Department of Materials and Metallurgical Engineering, Amirkabir University of Technology, 15875-4413, Tehran 15916-34311, Iran
[2]Condensed Matter and Materials Theory Division, Department of Physics, Chalmers University of Technology, SE-412 96 Gothenburg, Sweden
[3]Science Institute, University of Iceland, Dunhaga 3, IS-107 Reykjavik, Iceland
[4]Division of Space and Plasma Physics, School of Electrical Engineering and Computer Science, KTH Royal Institute of Technology, SE-100 44 Stockholm, Sweden
[5]GREMI UMR7344 CNRS, Université d'Orléans, BP6744, 45067 Orleans CEDEX 2, France

[a)]**Electronic mail:** movaffaq.kateb@chalmers.se

ABSTRACT

The detailed mechanism of bonding in the cold spray process has remained elusive for both experimental and theoretical parties. Adiabatic shear instability and hydrodynamic plasticity models have been so far the most popular explanations. Here, using molecular dynamics simulation, we investigate their validity at the nanoscale. The present study has potential applications in the fabrication of ultrathin layers in the electronics industry. For this aim, we considered Ti nanoparticles of different diameters and Si substrates of different orientations. It is shown that very high spray velocities are required for a jet to be observed at the nanoscale. We propose a method for thermostating the substrate that enables utilizing high spray velocities. For the first time, we demonstrate an oscillatory behavior in both the normal and radial stress components within the substrate that can propagate into the particle. We have shown that neither the adiabatic shear instability model nor the hydrodynamic plasticity model can be ignored at the nanoscale. In addition, the formation of a low-resistance titanium silicide proper for electronic application is illustrated.

I. INTRODUCTION

Cold spray[1,2] is a deposition method in which particles are accelerated toward a substrate by supersonic expansion of a gas stream. The term *cold* refers to the fact that, unlike thermal spray,[3] there is no phase change, especially melting, prior to the particle impact onto the substrate, and thus, the adhesion is solely dependent on the spray velocity (V_0) that produces strain rates on the order of 1/ns[1] during the impact. Despite the growing interest in the real-time imaging of the single particle collision,[2,4] the temporal and spatial resolution required for understanding the detailed mechanism is experimentally beyond the reach. Thus, our understanding of the cold spray process is limited to theories based on the postdeposition characterization.

To verify hypotheses regarding the detailed cold spray process mechanism, simulation and modeling have been shown to be promising (cf. Refs. 1, 5 and 6). In particular, the time scale in molecular dynamics (MD) simulations is highly compatible with that of the cold spray i.e., V_0 translates to 1–3 lattice parameters per ps and strain rates on the order of 100/ps can be achieved.[7,8] In addition, there is a growing interest in the nanoparticle cold spray technique.[9–13] MD simulations have been verified to capture nanoscale phenomena owing to their atomistic resolution.[14–17]

Several MD simulation studies have been conducted on the cold-spray process (cf. Ref. 6 and references therein). Probably, Gao *et al.*[18] were the first to demonstrate simulations of the cold spray process by MD. They pointed out that the process involves

partial melting behavior. In another interesting approach, Daneshian and Assadi[19] used the low-cost Lennard-Jones force field in 2D and modified its cut-off to model brittle particle impact on a rigid substrate. Their simple model showed a fair agreement with the analytical approach and captured many critical facts including plastic deformation below a certain size.

There have been efforts to study nanoparticle cold spray using MD simulations to achieve ultrathin, yet uniform, films, suitable for the electronics industry. It has been shown that deposition under an angle, namely, a larger off-normal angle (30°), increases the film uniformity.[20] However, the quality of the film, as measured by residual stress becomes inferior due to a reduction in the normal component of the spray velocity V_0.[21] Thus, one may need to increase the spray velocity V_0 beyond the current limits to reach optimum uniformity and stress.

The plastic deformation correlation with local temperature and their dependence on the spray velocity V_0 were demonstrated by Jami and Jabbarzadeh[7] using MD simulations. They also reported minimal changes in the particle size (2 and 20 nm), except for the fact that size-dependent melting temperature may contribute to the process. Later, they studied the TiO_2/Ti system using a relatively expensive force field.[8] They observed plastic deformation of brittle TiO_2 in agreement with the simple 2D model.[19] Rahmati *et al.*[22] studied a wide range of particle sizes (5–40 nm) for the Cu/Cu system and demonstrated localization of the dislocation network inside the particle next to the substrate. The possibility of mesoscale simulation and polycrystalline Al/Al system using quasi-course-grain has also been demonstrated.[23] However, they maintained their substrate temperature at 150 K to avoid stability issues.

Many of the above-mentioned studies are set up as proof of principle studies, so they consider a similar composition for both the nanoparticle and the substrate.[18,20–22,24] Such an assumption normally leads to nonrealistic interface behaviors. As we showed earlier,[25–27] for Cu/Cu deposition by various methods, film-substrate similarity might overestimate intermixing even with high accuracy force fields such as EAM.[28] Moreover, the energy barrier for recrystallization of a pure amorphous interface is negligible, which can exaggerate postimpact crystal recovery.[18,24,28]

While some studies were justly focused on the effect of the spray velocity V_0, they delivered the results in a limited velocity window 300–500 m/s, or even neglected the particle size effect (cf. Refs. 8 and 21). As pointed out by Pereira *et al.*[24], a spray velocity V_0 over 500 m/s is suggested to break surface oxide/contamination of Cu particles. Earlier, Assadi *et al.*[1] proposed $V_0 > 550$ m/s for *adiabatic shear instability* to occur for Cu. The low V_0 has probably been a technical issue associated with the lack of, or improper substrate thermostating, as hinted by Gao *et al.*[18] and Rahmati *et al.*[22] In the method section, we proposed utilizing a three-layer substrate scheme, a common method in high energy ion bombardment simulation, that allows performing cold spray at very high V_0. This is important because the drag force exerted by gas expansion is proportional to the particle's cross section or the surface area in general. However, the acceleration is inversely proportional to the particle's mass and thus to its volume. Assuming a spherical particle with diameter D, the acceleration becomes proportional to $1/D$. Therefore, smaller particles achieve higher ultimate velocities than larger ones.[1,29–31]

In the present work, we study cold spray deposition of a Ti nanoparticle onto a Si substrate. This is a very complex system due to the presence of metallic, covalent, and covalent-ionic bonds between TiTi, SiSi, and TiSi, respectively. Thus, one can expect a totally different chemistry than in the previous metal/metal system studies. Ti is a highly reactive metal that requires extra special considerations to be deposited by conventional thermal evaporation or sputtering. Thus, cold spray can be a unique alternative to minimize the oxide and nitride ratio. Rapid thermal annealing of Ti/Si results in reduced sheet resistance, which is desirable for interconnects in the semiconductor industry. One can skip the annealing step if increased mixing is achieved through adjusting the spray velocity V_0. For these reasons, we believe Ti/Si cold spray is important from both scientific and engineering points of view. Here, we focus on the single collision/deposition with an emphasis on the effect of V_0. Single particle collisions allow us to understand the bonding mechanism and have become popular in practice.[2] For the current study, we consider different substrate orientations as well as different particle sizes. The MD simulation method is described in Sec. II, the results are presented in Sec. III, and a summary is given in Sec. IV.

II. METHOD

Our MD simulations[32] were performed by Large-scale Atomic/Molecular Massively Parallel Simulator (LAMMPS)[33,34] code.[35] The three-body Tersoff force field was employed to model the entire interactions of the system. The general form of the Tersoff[36] potential is described by

$$U(r_{ij}) = f_c(r_{ij})\left[A_{ij}\exp(-\lambda_{ij}r_{ij}) - b_{ij}B_{ij}\exp(-\alpha_{ij}r_{ij})\right], \quad (1)$$

where r_{ij} is the distance between atom i and j; A_{ij}, B_{ij}, λ_{ij}, and α_{ij} are constant parameters; and f_c is the smoothing function near the cut-offs. b_{ij} is the main bond order term of the Tersoff potential that affects the attraction upon the changes in the bond angle, number of nearest neighbors, and their symmetry as follows:

$$b_{ij} = [1 + (\beta\zeta_{ij})^n]^{-\frac{1}{2n}} \quad (2)$$

in which β and n are constants and ζ_{ij} is given by

$$\zeta_{ij} = \sum f_c(r_{ij})g(\theta_{ijk})\exp[\lambda^m(r_{ij} - r_{ik})^m], \quad (3)$$

where the exponential term considers how central atom i energy due to atom j changes with its second nearest neighbor k and thus, λ and m are three-body constants. The angle θ_{ijk} enters as

$$g(\theta_{ijk}) = \left(1 + \left(\frac{c}{d}\right)^2 - \frac{c^2}{d^2 + (h - \cos\theta_{ijk})^2}\right)\gamma_{ijk}, \quad (4)$$

where c, d, h, and γ_{ijk} are constants. Note that some of these constants were only considered to adopt different existing formalisms, and thus, they are already known. We used the Tersoff parameters provided by Plummer and Tucker,[37] which was originally developed for the Ti_3SiC_2 MAX phase. Such a structure consists of a

sandwich of Si monolayers between titanium carbide (Ti_3C_2) layers. In particular, the force field models pure Ti and Si very well and predicts their interface energy with unique precision, making it suitable for very high strain rates. The set of parameters compatible with LAMMPS can be found in the supplementary material.

The substrate was assumed to be single crystal Si with nearly 100×100 Å^2 lateral dimensions and 50 Å thickness unless stated otherwise. We considered substrates with ⟨001⟩, ⟨011⟩, and ⟨111⟩ orientations along the growth direction (z). Each substrate was allowed to expand in the plane (xy) to reach zero stress at 300 K before the cold spray experiment. Similarly, particles were relaxed at 300 K in a large enough box that resembles isolation in a vacuum. This is a sensible choice since nanoparticles have a lower melting point than bulk. Thus, to fully leverage the benefits of cold spray, it is crucial to prevent their melting. We divided each substrate into fixed, thermostat, and surface atoms as explained elsewhere[25] and shown in Fig. 1. Briefly, the fixed layer is located at the bottom where we remove its net velocity but its atoms are allowed to vibrate naturally. The thermostat layer is meant to maintain the temperature of the surface layer at 300 K. The surface layer is thick enough so that particle collisions do not affect other layers.

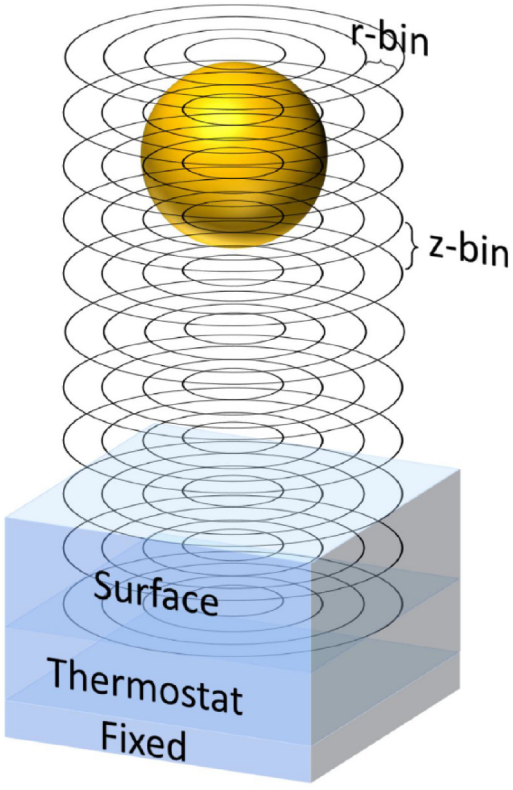

FIG. 1. Schematic illustration of the cylindrical bins used for spatial averaging of the per-atom stress tensor **σ**. Note that z-bins span a range that includes both the particle and substrate surface and r-bins are considered from the center to the extent of the substrate plane.

Such a scheme enables performing simulation at higher spray velocities V_0 than the earlier studies. Although many studies have omitted thermostating, there are reports where it has been included.[18,20,22] Gao *et al.*[18] considered the fixed layer unnecessary since they studied very small particles. Joshi and James[20] and Rahmati *et al.*[22] considered the fixed layer, but treated it as completely static, without the natural atomic vibrations present at finite temperature. In the Result section, we explain how their assumptions kept them away from reaching high spray velocities V_0 necessary for observation of the jet.

The Ti nanoparticles were assumed to have an icosahedral (ico) shape with diameters ranging from 0.9 to 4.1 nm. Each particle was individually relaxed at 300 K using the Nosé–Hoover thermostat that generates samples from the canonical ensemble (NVT). Further details on the choice of shape and relaxation can be found elsewhere.[15,16]

For the time integration of the equation of motion, we follow the velocity Verlet algorithm[14,38] using 0.5 fs timestep in both relaxations and the collision. The latter was performed by sampling from the microcanonical (NVE) ensemble. The thermostat layer was controlled by the Langevin thermostat[39] with a damping of 1 fs and considering surface layer temperature. Such a small damping enables us to study very high spray velocity V_0 or up to 3000 m/s.

For quantitative comparison of intermixing, we calculated the partial radial distribution function, $g_{ij}(r)$.[40] However, the original notation is based on the binary mixtures being homogeneous. For an earlier study, we introduced a slightly modified version for an interface with continuous composition profile,[26] which will be used here.

The local microstructure is analyzed by polyhedral template matching (PTM).[41] Briefly, it generates a polyhedral shape using the first nearest neighbors and compares it to the desired template (s). It is insensitive to the interatomic distances used by other methods and thus immune to the error caused by strain and thermal fluctuation. However, similar to other methods, it distinguishes surface atoms as disordered, labeled as non, because of insufficient number of first nearest neighbors.[15,25] We considered diamond cubic (dia), face-centered cubic (fcc), hexagonal closed packed (hcp), and ico templates.

We utilized the open visual tool (Ovito)[42] code[43] to generate atomistic illustrations as well as for postprocessing.

In the MD framework, per-atom stress tensor (**σ**) is calculated according to the *virial* notation

$$\sigma_{pq} = -\frac{1}{\Omega_i}\left(m_i v_p v_q + \sum_{i \neq j} f_{ij} r_{ij}\right), \tag{5}$$

where σ_{pq} is an element of **σ** tensor with p and q being Cartesian coordinates; m and Ω are atomic mass and volume of the reference atom i, respectively; $v_{p/q}$ is the velocity component of atom i; and f_{ij} is the force exerted by atom j on atom i. The above definition can be understood as an outcome of the equation state for the ideal gas plus excess pressure term due to interatomic forces.

In order to convert the stress tensor **σ** in Cartesian coordinates into cylindrical coordinates, we first must determine in-plane angle θ. This can be simplified when the particle and substrate are

centered at $x = y = 0$, and the particle moves along the z-axis as

$$\theta = \arctan(y/x), \tag{6}$$

where x and y are the atom coordinates and thus, an angle θ will be assigned to each atom. Now, one can determine per-atom stress in cylindrical coordinates

$$\begin{aligned}
\sigma_{rr} &= \cos^2\theta\sigma_{xx} + 2\cos\theta\sin\theta\sigma_{xy} + \sin^2\theta\sigma_{yy},\\
\sigma_{r\theta} &= \cos\theta\sin\theta(\sigma_{yy} - \sigma_{xx}) + (\cos^2\theta - \sin^2\theta)\sigma_{xy},\\
\sigma_{rz} &= \cos\theta\sigma_{xz} + \sin\theta\sigma_{yz},\\
\sigma_{\theta\theta} &= \sin^2\theta\sigma_{xx} - 2\cos\theta\sin\theta\sigma_{xy} + \cos^2\theta\sigma_{yy},\\
\sigma_{\theta z} &= -\sin\theta\sigma_{xz} + \cos\theta\sigma_{yz},\\
\sigma_{zz} &= \sigma_{zz},
\end{aligned} \tag{7}$$

where similar and dissimilar subscript denote normal and shear components of the stress tensor $\boldsymbol{\sigma}$. Regardless of the coordinate system, interpreting per-atom stress tensors is not an easy task. To provide a simpler view of the stress distribution, we averaged per-atom values obtained by Eq. (7) in cylindrical bins schematically as shown in Fig. 1. We considered five radial bins (rings) of ~1 nm width, labeled by the average r as $\bar{r} = 0.5$, 1.6, 2.7, 3.7, and 4.8 nm, and 130 bins along the z-axis (0.1 nm each). We have tested several bin-sizes along the z-axis, and it seems one may sacrifice important features above 0.5 nm. Within each bin, the $\boldsymbol{\sigma}$ tensor is averaged over all atoms and time-averaged for 100 timestep.

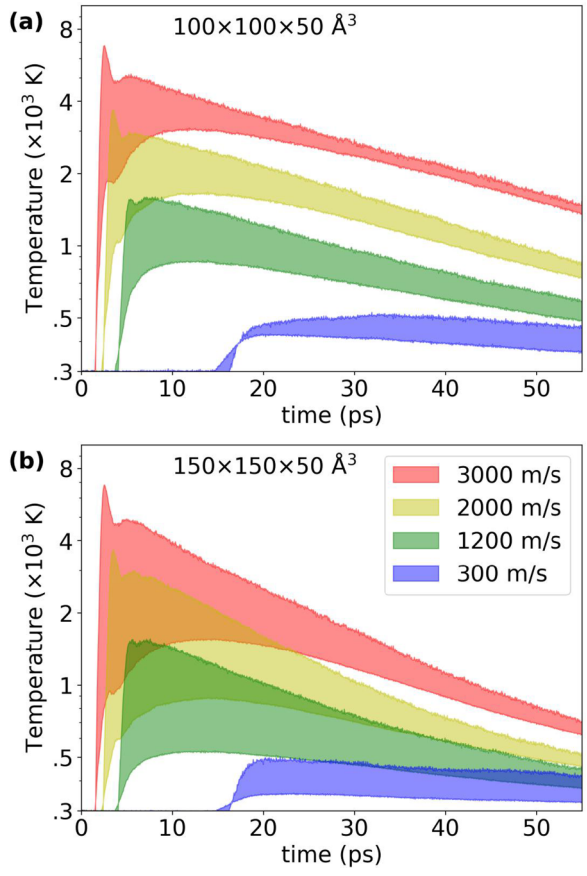

FIG. 2. The temporal variation of T_{par} (top limit) and T_{sur} (bottom limit) with varying V_0 for a 4.1 nm diameter Ti ico particle onto a (100) Si substrate with (a) 100 × 100 and (b) 150 × 150 Å^2 lateral dimensions. Note that the vertical axis is plotted in the semilog.

III. RESULTS

A. Caloric response

Figure 2 shows the temporal variation of temperature for various spray velocities V_0 for a 4.1 nm diameter Ti ico particle onto (100) Si substrate. The top and bottom limits denote particle temperature (T_{par}) and surface layer temperature (T_{sur}), respectively. This defines the shaded area denoting the temperature difference between T_{par} and T_{sur}. Since the surface layer is in contact with the thermostat (cf. Fig. 1) its temperature is much better controlled and it stands a few hundred K below that of the particle. Figure 2(a) shows the result for a substrate with 100 × 100 Å^2 lateral dimension in which we first observed a jet for V_0 of 3000 m/s. In order to make sure the jet is not an artifact of limited heat dissipation we repeated the numerical experiment with a larger substrate.

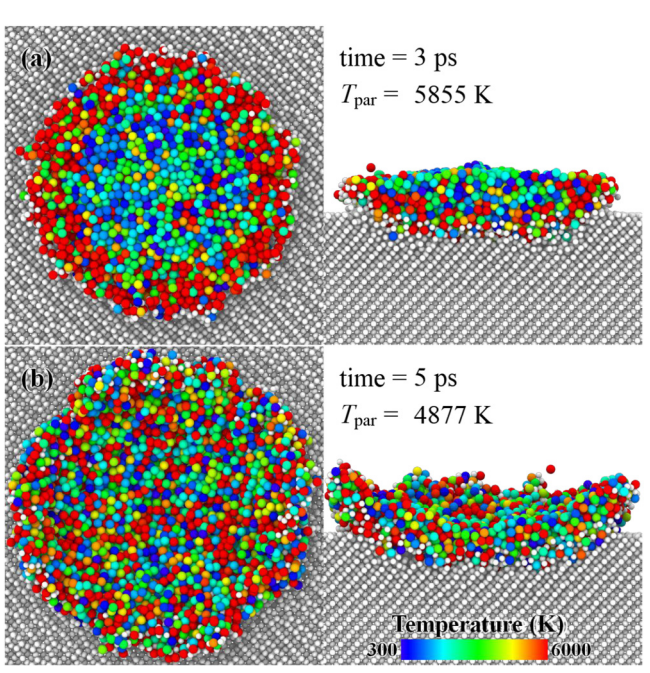

FIG. 3. Atomistic illustrations of 4.1 nm diameter Ti ico particle onto a (100) Si substrate with $V_0 = 3000$ m/s. Particle top and side views for (a) flattening and (b) jet corresponding to the first and second T_{par} peaks, respectively. For the side view, we made a slice through the middle of the particle. Substrate atoms are shown in gray for illustration purposes.

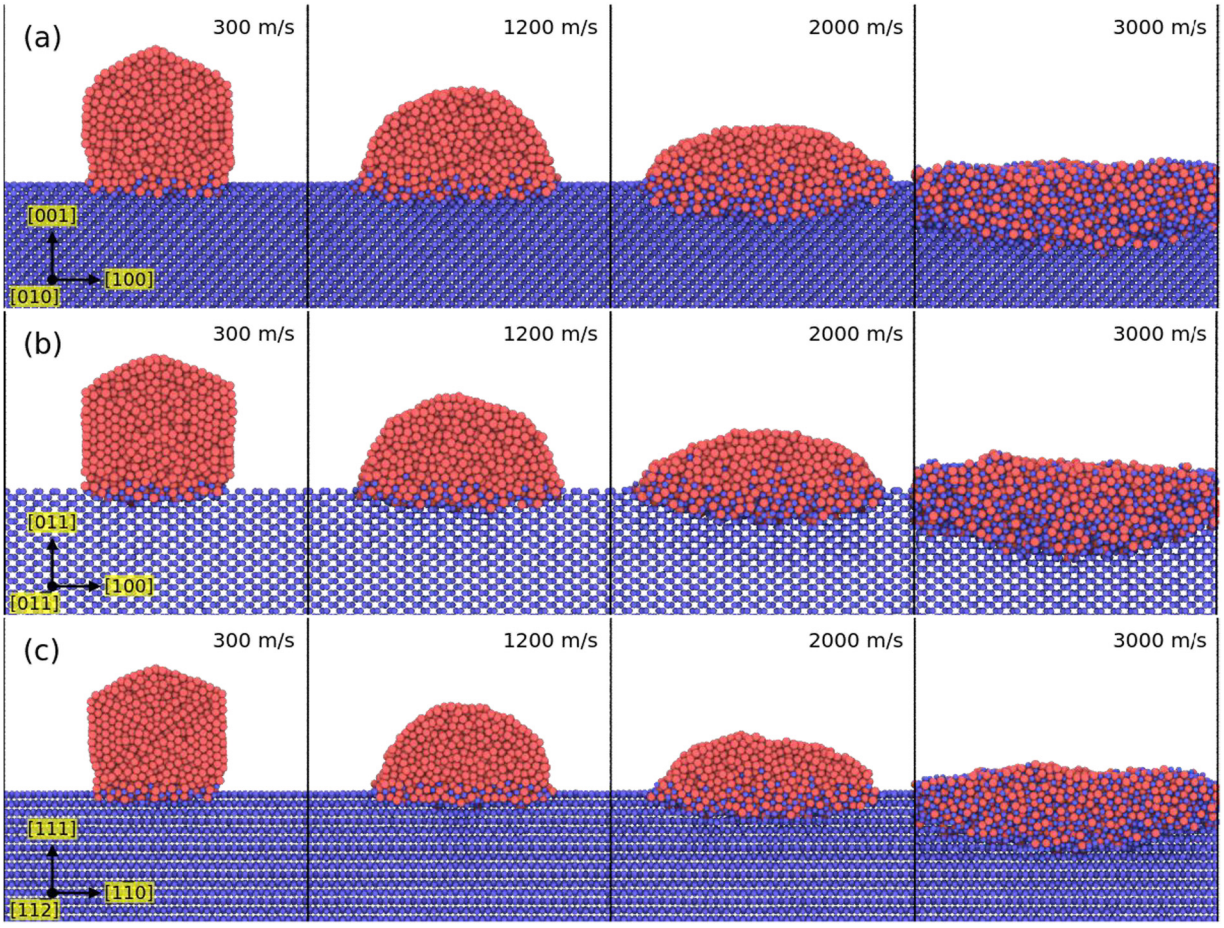

FIG. 4. Dependence of interdiffusion on the spray velocity V_0 for a 4.1 nm diameter Ti ico particle on (a) (100), (b) (110), and (c) (111) Si substrates. All snapshots depict a slice in the middle of particles.

For the larger substrate, shown in Fig. 2(b), the contact between the surface layer and the thermostat is larger, and consequently, T_{sur} is even lower. However, the substrate dimensions do not change the early-stage variation of the particle temperature T_{par}. At this stage, which will be referred to as impact hereafter, T_{par} is only determined by the spray velocity V_0. Upon the impact, two peaks are observed in the T_{par} at the higher velocities 1200–3000 m/s. There is also a visible change in T_{sur} corresponding to the first peak in T_{par}. The range of temperatures observed here is in agreement with the findings of Colla *et al.*[44] but well below what was observed by Cleveland and Landman.[45]

The real-time comparison with the MD trajectory (Fig. 3) indicates that the first and second T_{par} peaks are associated with particle *flattening* and *jet*, respectively. The fact that T_{par} does not change with better heat dissipation (larger substrate) and observation of a jet are solid pieces of evidence for adiabatic shear instability.[1] We did not observe the jet for spray velocities below 3000 m/s. As previously mentioned, some studies have found thermostating essential to achieve high spray velocities V_0.[18,20,22] However, due to slightly different conditions in the fixed layer and thermostat damping, we were able to reach the spray velocity V_0 necessary for jet ejection.

In the postcollision regime, T_{par} decreases monotonically, which is a characteristic of heat conduction into the surface layer. Similarly, T_{sur} depends on the heat removed from the surface by the thermostat layer. A larger substrate area improves the heat dissipation from the surface and lowers T_{sur}. Consequently, T_{par} drops faster, as seen in Fig. 2(b). On the other hand, T_{sur} still approaches its maximum (T_{sur}^{max}) after the jet. As T_{sur} without proper thermostating is uninformative, earlier studies sufficed to report T_{par}, cf. Refs. 7 and 8, and T_{sur} has been barely reported.[18] For Au spray on Au, Gao *et al.*[18] observed peak in T_{sur} with a constant delay after the collision, independent of V_0. As can be seen here, the time between first T_{par} peak and T_{sur}^{max} increases with an increase in V_0. Such a gradual increase in T_{sur} is associated with the ongoing intermixing, i.e., titanium silicide layer thickening. It is also worth mentioning that at spray velocity of 300 m/s, we observed landing, i.e.,

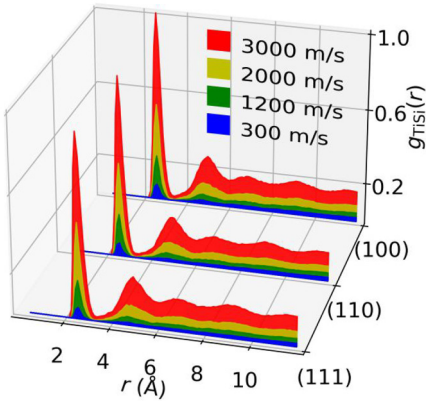

FIG. 5. Partial radial distribution $g(r)$ for TiSi after spraying 4.1 nm diameter Ti ico particles onto (100), (110), and (111) Si substrates.

without the plastic deformation. This is phenomenologically different than the impact at higher V_0. Thus, one cannot expect impact peaks in T_{par} at low V_0, as observed in earlier studies (cf. Refs. 7 and 8). We obtained similar behavior for higher surface densities, i.e., 29% and 13% higher, corresponding to (110) and (111) Si substrates, respectively (cf. Fig. S1 in supplementary material).

B. Bonding

Figure 4 shows the dependence of interdiffusion on the spray velocity V_0, for a 4.1 nm Ti diameter ico particle on (100), (110), and (111) Si substrates. Considering the topmost Si atom in blue and the lowermost Ti atom in red, one can clearly see that the diffusion decreases with higher planar densities. This is even true at 3000 m/s where severe intermixing occurs.

While Fig. 4 clearly depicts the depth of diffusion, complementary information on the interdiffusion can be obtained by exploring the partial radial distribution, $g(r)$. Figure 5 shows $g_{TiSi}(r)$

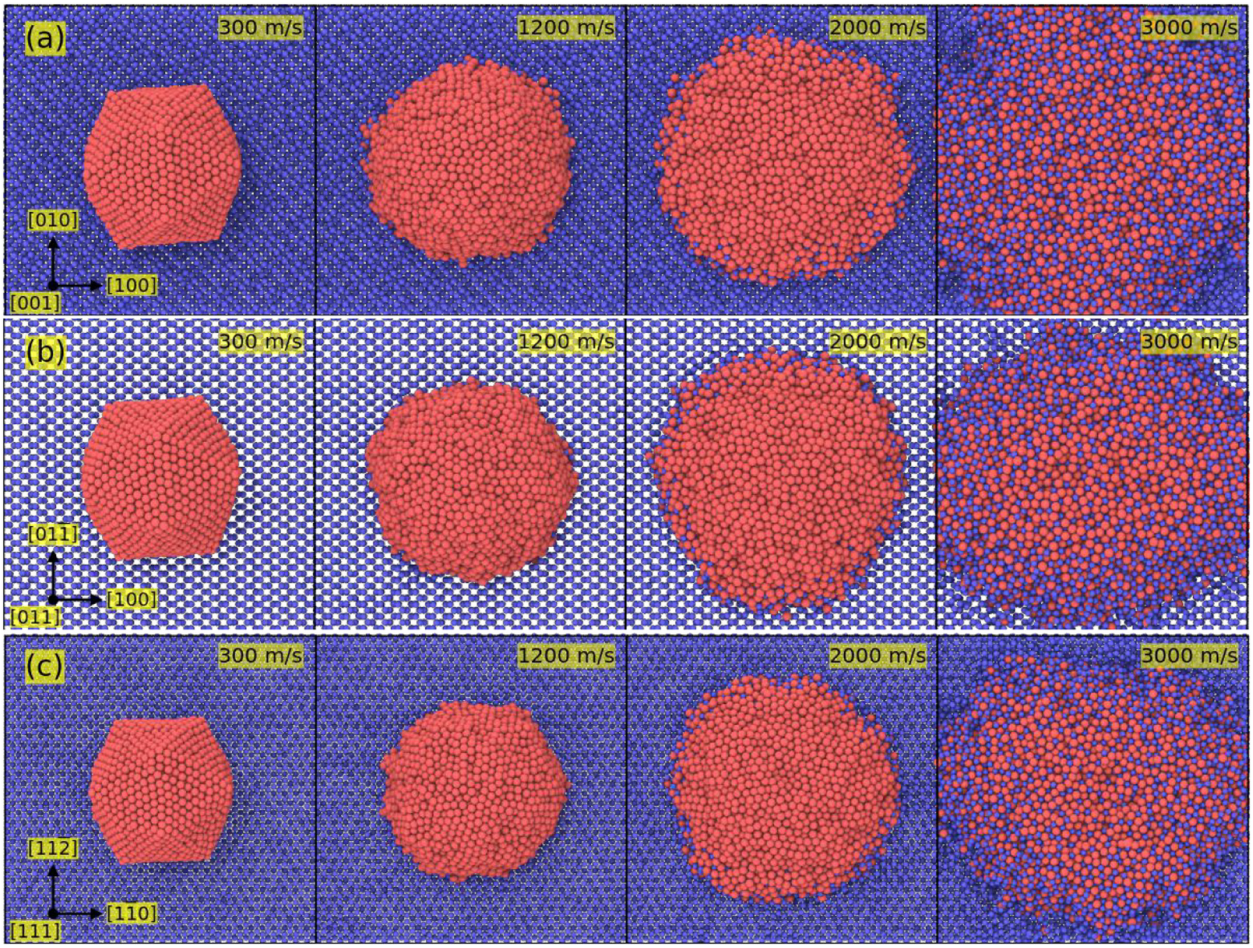

FIG. 6. Dependence of the lateral spreading on the spray velocity V_0 for 4.1 nm diameter Ti ico particle spreading atop (a) (100), (b) (110), and (c) (111) Si substrates.

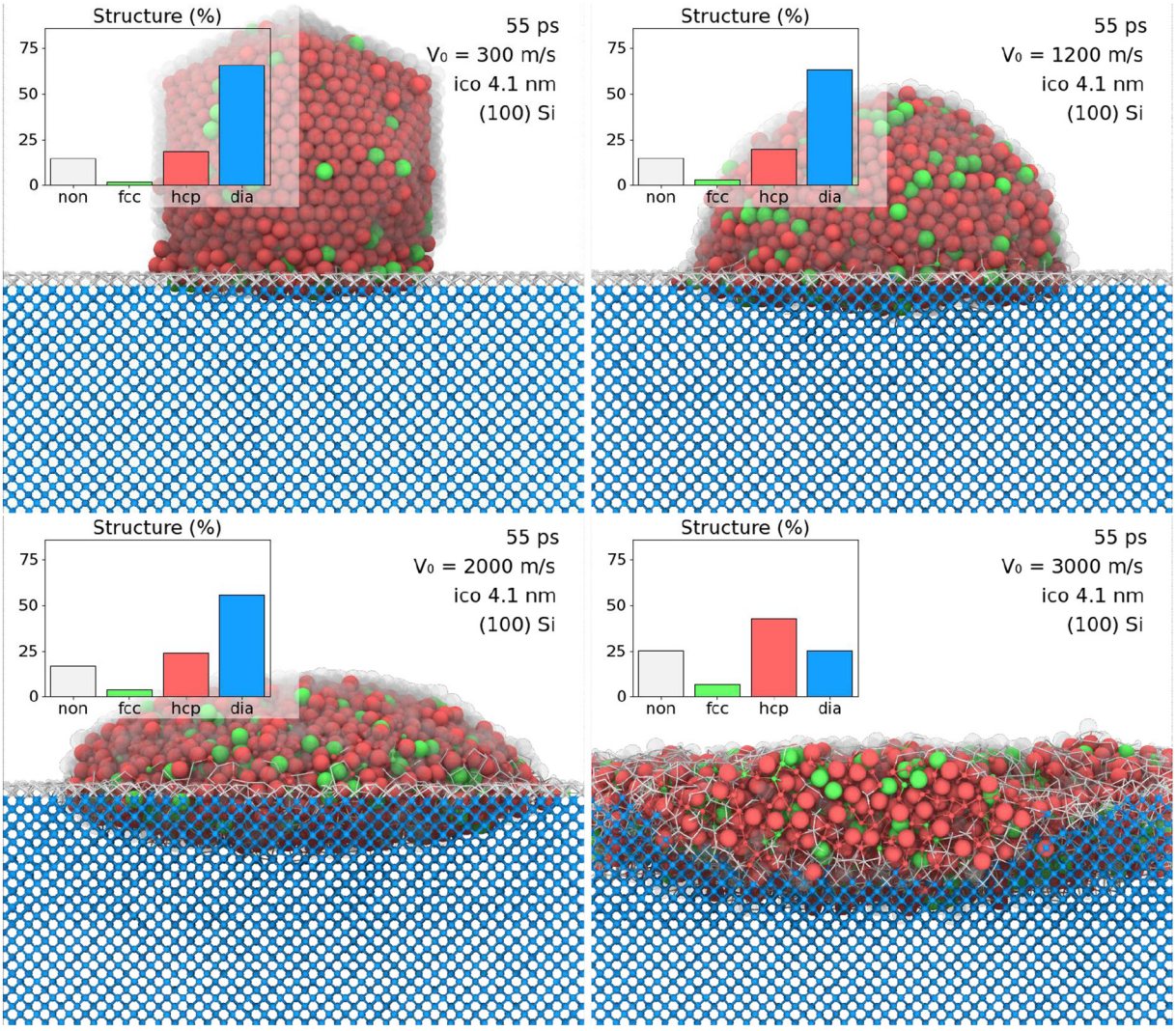

FIG. 7. The result of PTM for 4.1 nm diameter Ti ico particle spray at different V_0 onto (100) Si substrate. Substrate atoms are shown with smaller diameters also surface and disordered atoms are presented as semi-transparent in white.

for 4.1 nm diameter Ti ico particle onto different Si substrates. Looking at the major peak (at $r = 2.5$ Å), one can see immediately that higher V_0 leads to more TiSi bonds (first nearest neighbors). It can be seen that there is almost no difference between $g_{\mathrm{TiSi}}(r)$ obtained with different substrates. One may think, this is inconsistent with the diffusion depth observed in Fig. 4. However, as explained elsewhere,[16] $g_{\mathrm{TiSi}}(r)$ is not sensitive to the detailed geometry. As a matter of fact, when the planar density is higher, a shorter diffusion depth will produce the same number of TiSi pairs. Thus, it is necessary to compare $g(r)$ with other information to acquire a full picture of the process.

There have been efforts to predict critical velocity V_{cr} for bonding to occur based on the thermo-mechanical properties of the materials.[1,30,46] Schmidt *et al.*[30] introduced, assuming a simple empirical model, $V_{\mathrm{cr}} = FD^{-n}$ at constant temperature, with F and n being fitting parameters and D being particle diameter. Recently, Dowding *et al.*[47] fitted F and n for Ti particles of 5–50 μm in diameter to be 1280 $\frac{\mathrm{m/s}}{\mu\mathrm{m}^{-n}}$ and 0.21, respectively. Extrapolating to 4.1 nm diameter particle size, a critical velocity of 4060 m/s can be estimated. This is in close agreement with the jet we observed at 3000 m/s, considering the fact that we have ideally clean surfaces while experimental studies suffer from this point. We would like to remark that meeting the size and velocity criteria is necessary for adiabatic shear instability. Outside these choices, bonding may be achieved but with a different mechanism. For instance, although Au has a very large critical diameter, Gao *et al.*[18] observed

successful bonding of its nanoparticles, attributing this to partial melting during the process.

C. Spreading

In practice, the initial particle diameter (D) is unknown, thus the measurement of lateral spreading (w) and height (h) can be used to determine $D = \sqrt[3]{w^2 h}$.[48] In simulations, D is known, and thus, the spreading ratio w/D can be determined as a measure of strain. Figure 6 shows the variation of lateral spreading with V_0 for 4.1 nm Ti diameter ico particle over (100), (110), and (111) Si substrates. By fitting a circle to the outermost Ti atoms, as explained in the supplementary material, spreading ratios of 1.3, 1.6, 2.0 and 2.5 were obtained at 300–3000 m/s, with negligible changes on different substrates. It is worth mentioning that the particle nearly keeps the ico shape at V_0 of 300 m/s. Considering the fivefold symmetric corners in ico, they are still observable at the particle's top for 1200 m/s. At 2000 m/s, the corners' symmetry becomes vague, while at 3000 m/s, mixing with the substrate takes over. This is consistent with the earlier experimental[4] and simulation[22] studies that limit the plastic deformation to the bottom side of the particle. The spreading ratio is a rough measure of the strain, meaning it represents an average value of local strains. The fact that the particle's top experiences smaller deformation indicates that the local strain at the interface is much larger than the spreading ratio.

D. Microstructure

Figure 7 shows a PTM analysis of 4.1 nm diameter Ti ico particles on a (100) Si substrate, delivered at different spray velocities V_0. Note that we only included the particle and the surface layer in the PTM calculation. It can be seen that the ratio of non, fcc, and hcp structures increase with increased spray velocity V_0 at the cost of a reduction in the dia structure. At spray velocity of 3000 m/s, the dia ratio reaches that of non and is well below that of hcp. The former can be expected in an energetic impact, while the latter seems unpredicted. This can be explained considering the $TiSi_2$ structure as follows.

In the semiconductor industry, $TiSi_2$ is known to have C54 and C49 structures.[49,50] The development of the high-resistivity (60–90 μΩ cm) metastable C49 phase and its subsequent transformation into the low-resistivity (12–20 Ω cm) C54 phase is of significant interest from both technological and scientific perspectives.[50] Here, we emphasize on face-centered orthorhombic (C54) $TiSi_2$ as shown in Fig. 8. In the C54 structure, each Ti atom is surrounded by 10 Si atoms at 2.55–2.78 Å distance, while Si atoms have five Ti and five Si nearest neighbors with Si–Si distance of 2.52–2.79 Å. The existence of four bond lengths makes the PTM characterization of $TiSi_2$ nearly impossible. However, it can be seen that the xy plane (top-left) is highly compatible with the hcp basal plane. Thus, it is very likely that C54 is characterized as an hcp-like structure.

E. Stress

Figure 9 shows the variation of the normal stress component σ_{zz} for 4.1 nm diameter Ti ico particle on the (001) Si substrate. The figure includes four panels, one for each given spray velocity

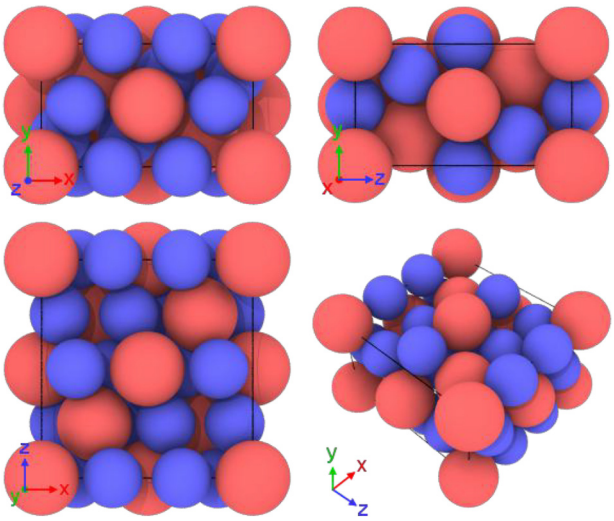

FIG. 8. A C54 unit cell (8.2671 × 4.800 × 8.5505 Å^3) of $TiSi_2$ with red (bigger) and blue (smaller) being Ti and Si, respectively. It is classified in the orthorhombic category with the oF24 Pearson symbol or Fddd space group. Note, how the xy plane (top-left) is compatible with the hcp basal plane.

V_0 (labeled on top), and within each panel, there are five subplots corresponding to the rings ($\bar{r} = 0.5$, 1.6, 2.7, 3.7, and 4.8 nm, as indicated on the right side). Here, $z \leq 0$ corresponds to the substrate surface and the top branch ($z > 0$) gradually approaching the substrate indicates the particle. Although both fcc and hcp structures have been reported for Ti nanoparticles,[51] the hcp remains the most stable phase at 300 K. Here, we chose the ico shape, which predominantly exhibits a fcc structure, as it most closely resembles a spherical shape while still presenting similar corners and facets. However, ico shape produces compressive stress in the core and tensile stress at the particle's surface. Before the collision, at 300 m/s, the stress component σ_{zz} at the particle's surface ($\bar{r} = 2.7$ nm) is tensile (in red), whereas in the particle's core, it is compressive ($\bar{r} = 0.5$ and 1.6 nm). As V_0 increases, the stress component σ_{zz} shifts toward a more compressive regime.

As expected, a particle impact introduces a compressive pulse into the substrate. The impact pulse appears as blue ($z < 0$) when the particle meets the substrate and its intensity and duration depend on the spray velocity V_0. For instance, at 300 m/s, the impact pulse appears very weak (pale blue) at $\bar{r} = 3.7$ nm, while at higher V_0, it can propagate to the outermost ring. In addition, the duration of the impact pulse is shorter for higher V_0 but more compressive (darker). It can be seen that almost always the normal stress component σ_{zz} shows an oscillatory behavior, i.e., the impact pulse is followed by a red one and so on, those are clearly depicted for spray velocity of 2000 m/s at different $\bar{r}$. Earlier, Hassani-Gangaraj *et al.*[46] had argued against the adiabatic shear instability mechanism of bonding, originally proposed by Assadi *et al.*[1] Instead, they suggested hydrodynamic plasticity at the interface that is induced by pressure waves. This is still an ongoing debate (cf. Refs. 52 and 53), but here for the first time, we

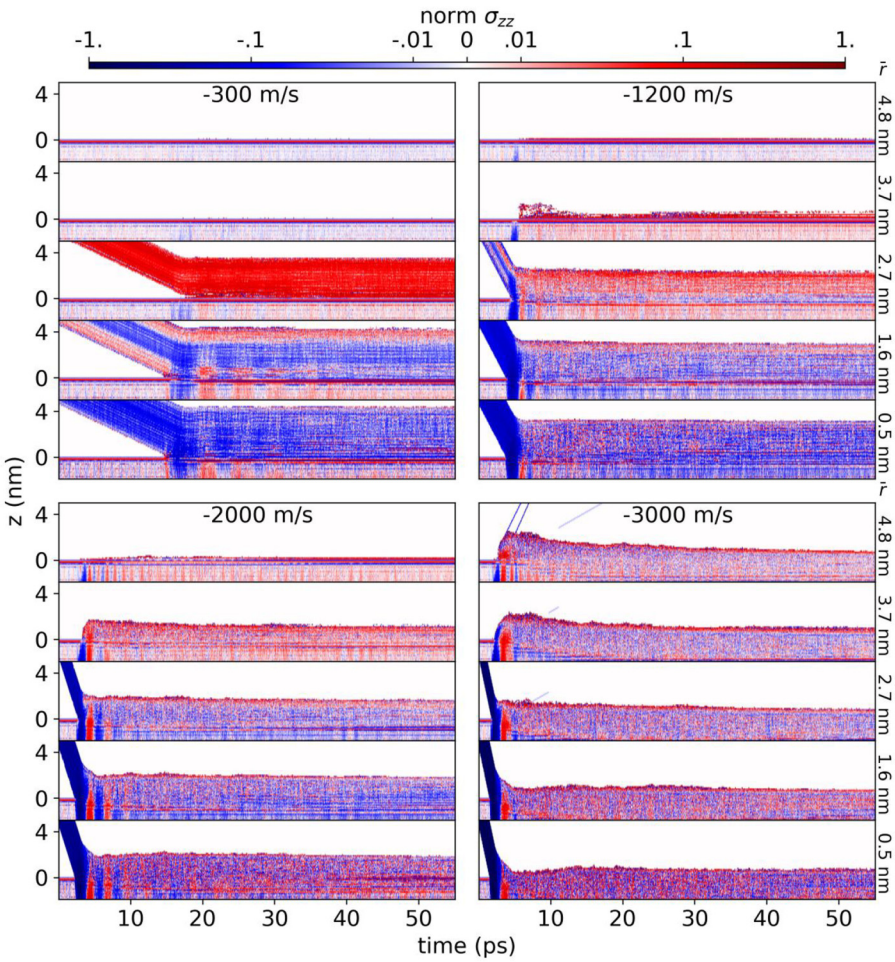

FIG. 9. Variation of the normal stress component σ_{zz} pattern by increase in V_0 for a 4.1 nm diameter ico particle and (001) Si substrate. Note that the colorbar is in the logscale outside ± 0.01.

demonstrate pressure waves which we refer to as stress oscillations. We believe the impact pulse produces a longitudinal (with respect to the substrate normal) acoustic wave for the following reasons: First, it is mostly incoherent at the interface ($z = 0$). Second, it lasts longer on the substrate than the particle due to the well-defined lattice. Last but not of least importance, it decays faster with higher residual stress (darker red and blue dots).

The blue lines in the outer rings, observed for spray velocity of 3000 m/s, indicate jet ejection. Regardless of the detailed mechanism,[1,46] it appears that the jet has been ruled out as the necessary characteristics of bonding.[52,53] We observed bonding for the different V_0 but only observed the jet at 3000 m/s in agreement with above-mentioned studies. Here we did not observe the rebound but we hypothesize the long-lasting normal stress component σ_{zz} oscillations to be responsible for the rebound.

We would like to remark that, while earlier studies consider an overall stress picture (cf. Refs. 7, 8, and 21) here we focused on the localized aspect that has been barely discussed.[1,54] For instance, at spray velocity of 300 m/s the substrate and the particle present different normal stress component σ_{zz}, above and below $z = 0$. For higher V_0 we observe a more uniform normal stress component σ_{zz} along the growth direction (z). Regardless of the velocity V_0, however, the normal stress component σ_{zz} is more compressive in the inner rings and *vice versa*. As pointed out earlier, an issue with the same particle and substrate is neglecting the interface effects. Here, it can be clearly seen that when moving along the z-direction, the normal stress component σ_{zz} becomes discontinuous at the particle-substrate interface. The only exception is that at spray velocity of 3000 m/s, where severe intermixing occurs, i.e., we were unable to locate a cluster of pure Ti.

The variation of the radial stress component σ_{rr} at different values of V_0 is depicted in Fig. 10 for a 4.1 nm diameter ico particle on the (001) Si substrate. Before the collision, regardless of V_0 and $\bar{r}$, the radial stress component σ_{rr} is always tensile (red) at the particle surface and compressive in the core. The topmost layer ($z_{\max}$) remains tensile even after the collision. Unlike for the normal stress component σ_{zz} case, collision-induced oscillations in the radial stress component σ_{rr} are barely symmetric and overall compressive. In the particle and interface, however, the radial stress component σ_{rr} presents a mixed state both tensile and compressive (red and

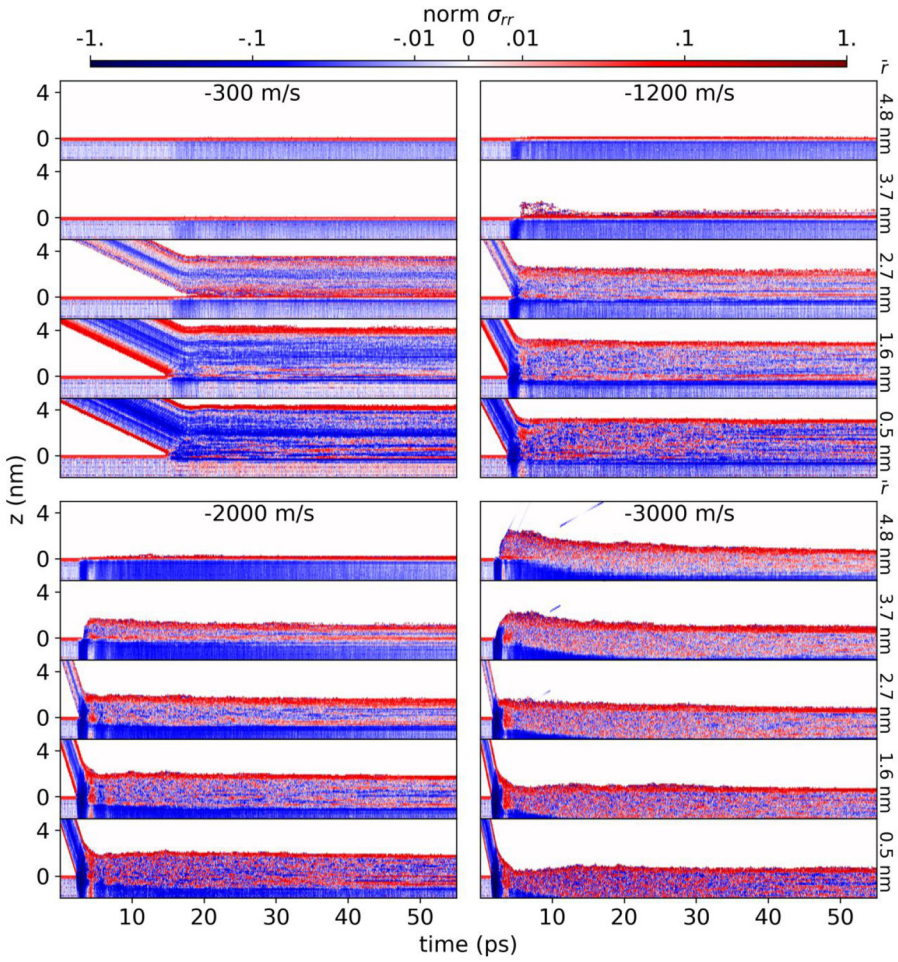

FIG. 10. Variation of the radial stress component σ_{rr} pattern by increase in V_0 for a 4.1 nm diameter Ti ico particle onto a (001) Si substrate. Note that the colorbar is in the logscale outside ± 0.01.

blue). Similar to the normal stress component σ_{zz}, by probing along the z-direction, the radial stress component σ_{rr} shows a discontinuity at the interface. However, the effect of V_0 on the radial stress component σ_{rr} is different than on the normal stress component σ_{zz}. Here, higher V_0 shift the substrate's radial stress component σ_{rr} toward more compression while its effect on the particle is the opposite. Thus, as V_0 increases, the slope of the radial stress component σ_{rr} at the interface increases.

F. Size-dependence

Figure 11 shows the variation of lateral spreading with the diameter of the Ti ico particle and the spray velocity V_0. For each particle size, denoted on top, four different spray velocities V_0 are shown as a quadrant. It can be seen that higher velocities are really ineffective in increasing the lateral spreading for the smallest particle, here 0.9 nm in diameter. However, for larger particles, increase in the lateral spreading with higher V_0 is evident.

Furthermore, we calculated the spreading ratio as shown in Fig. 12. It can be seen that the variation in the particle size is nearly monotonic except for the largest particle. The ratios consist of reducing, constant and increasing trends. A lower V_0 gives a nearly reducing ratio, while higher ones give more weight to the constant and increasing trends. To clarify whether or not a higher spreading ratio for 4.1 nm diameter particle is an artifact, we compared the results for different substrate sizes. We observed a negligible difference in the ratio between 100×100 and 150×150 Å^2 substrate sizes. In addition, we plotted the 4.1 nm results on the (110) and (111) Si substrates using square and triangle symbols, respectively. Again the result conforms with that for the (100) Si substrate, indicated by circles. We also compared different substrate dimensions (not shown here) and obtained similar results. Thus, the step change in the spreading ratio must be associated with the crossing of a critical diameter (D_{cr}) where adiabatic heating becomes dominating giving rise to plastic deformation. Schmidt *et al.*[30] defined D_{cr} as a diameter above which thermal diffusion is slow enough for adiabatic shear instability to appear at the particle surface. They introduced $D_{cr} = 36\kappa/C_p\rho V_0$ with κ, C_p and ρ being thermal conductivity, heat capacity, and density of the particle. For typical Ti deposition spray velocities, their model leads to $D_{cr} = 400$ nm. However, the V_0 term in the denominator enables reducing the D_{cr} using higher V_0 such as in this study.

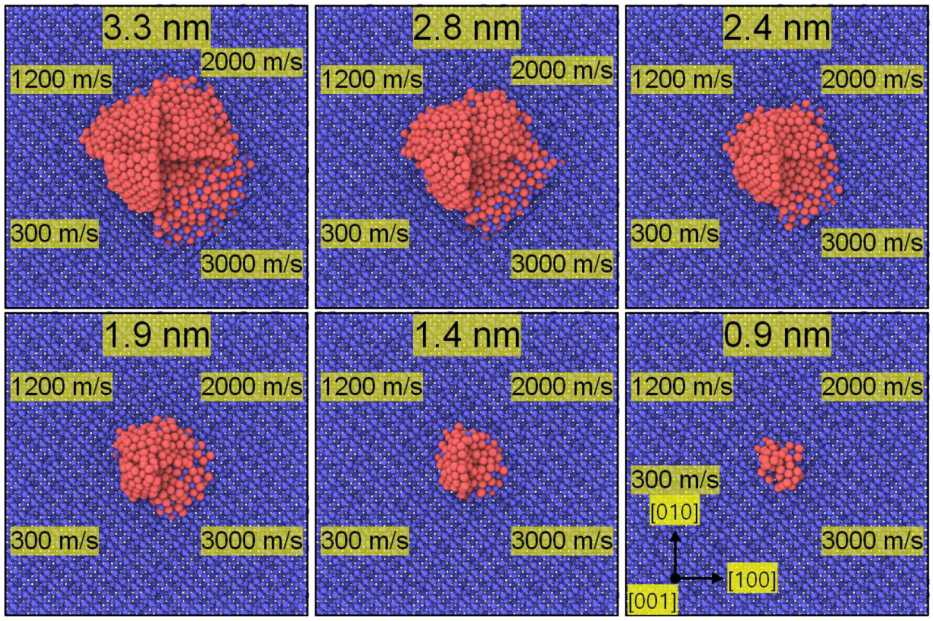

FIG. 11. The dependence of lateral spreading on the size of the Ti ico particle. For each particle, different spray velocities V_0 are shown in a quadrant.

Figure 13 shows the variation of TiSi partial radial distribution $g(r)$ with ico particle size. It can be seen that for the smallest ico particle (0.9 nm) different V_0 does not change the intermixing. The difference between $g(r)$ due to variation in V_0 is very small for the 1.4 nm diameter particle but its influence gradually increases with increased particle size until it becomes significant for the largest particle, here 4.1 nm in diameter. Thus, a higher V_0 becomes less important for the smaller particles.

Figure 14 shows the variation of T_{par} and T_{sur} with different spray velocities V_0 and particle sizes. Here the top and bottom limits denote T_{par} and T_{sur}, respectively, and their difference is shaded. One can see immediately that T_{sur}^{max} increases with increased particle size, while T_{par}^{max} is independent of the particle size, and only dependent on the spray velocity V_0. Consider the temperature as $T = \frac{2}{3} k_B \langle \mathcal{K} \rangle$ where the average kinetic energy is $\langle \mathcal{K} \rangle = \frac{1}{2} m V_0^2$ assuming adiabatic condition, at the early stage of impact. Thus, the particle's temperature is directly proportional to V_0 without being dependent on the number of atoms in the particle. The only exception is for spray velocity of 300 m/s as T_{par}^{max} decreases with increased particle size. Earlier, Hassani-Gangaraj *et al.*[53] reported increased temperature at the particle's perimeter, where the jet is expected, for larger particles. Note that here we plot

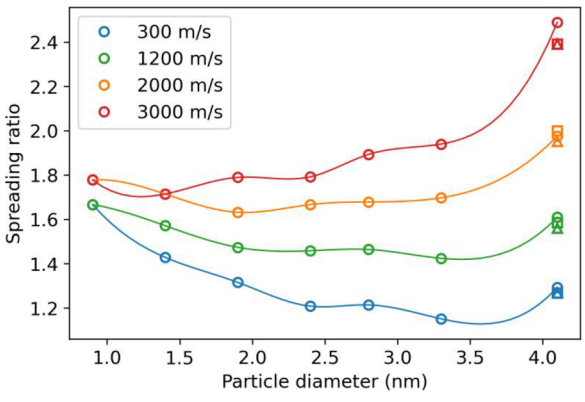

FIG. 12. Variation of the spreading ratio with the particle size and V_0. The lines are cubic splines to guide the eye. The circles, squares, and triangles denote results on (100), (110), and (111) Si substrates, respectively.

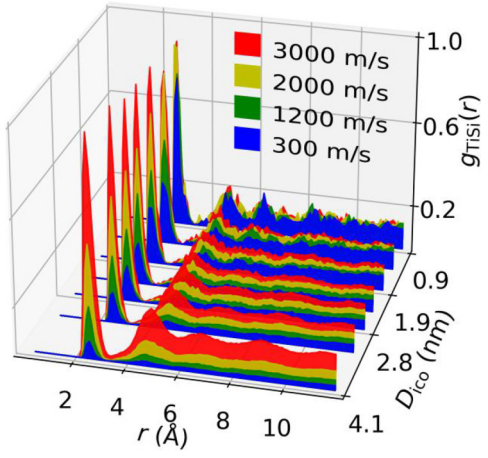

FIG. 13. Partial radial distribution $g(r)$ for TiSi after spraying Ti ico particles of different diameters at different spray velocity V_0 onto the (100) Si substrate.

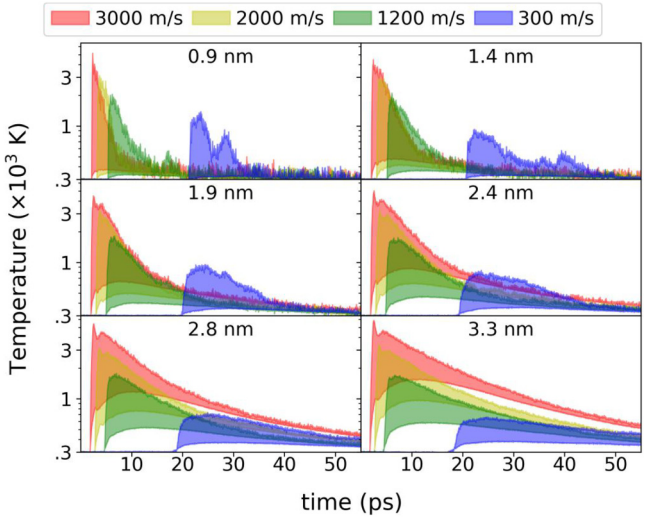

FIG. 14. The temporal variation of the T_{par} (top limit) and T_{sur} (bottom limit) with varying spray velocity V_0 for Ti ico particles of various diameters onto a (100) Si substrate. Note that the vertical axis is plotted in the semilog.

the average particle's temperature. The atomistic temperature, cf. Fig. 3(a), indicates that during the flattening stage particle's perimeter has a higher temperature.

Figure 15 shows the flattening ratio, $1 - h/D$, for different particle size and V_0. It can be seen that, unlike the spreading ratio, the step change at 4.1 nm is not always present. For adiabatic shear instability strains $\varepsilon > 4$[1] and 4.5[4] has been proposed using the Lagrangian and Eulerian finite element simulations. Comparing these numbers to the figure it appears that they refer to local values while the flatting ratio gives an average strain. For instance, the highest value here 0.7 corresponds to a final height of ∼1 nm. However, in-plane displacement of atoms can be much larger (cf. Fig. S3 of the supplementary material).

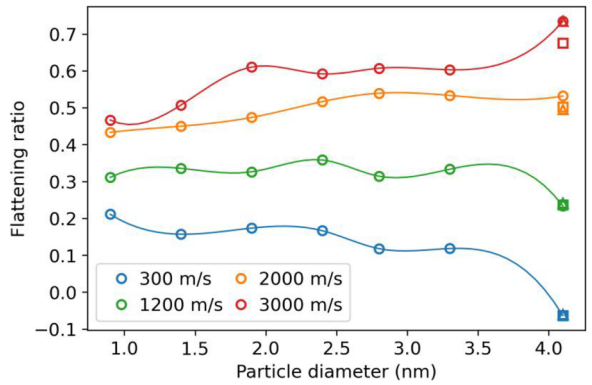

FIG. 15. Variation of flattening ratio with the particle size and spray velocity V_0. The lines are cubic splines to guide the eye. The circles, squares, and triangles denote results on (100), (110), and (111) Si substrates, respectively.

IV. CONCLUSION

We demonstrated cold spray of Ti nanoparticles (0.9–4.1 nm in diameter) onto a Si substrate over a wide range of spray velocities V_0, using molecular dynamics simulations. By proper choice of the thermostat layer and its damping, it is possible to model spray velocities V_0 up to 3000 m/s, which is necessary for the observation of adiabatic shear instability at the nanoscale. It is shown that, thanks to the ideally clean surfaces, bonding can be achieved over a wide range of spray velocities V_0 and particle sizes. However, for adiabatic shear instability to occur, one needs at least a 4.1 nm diameter particle at 3000 m/s where a jet can be clearly observed. Here, we have been able to detect D_{cr}, thanks to a step change in the spreading ratio, w/D, while other strain measures, such as flattening, may not always show such a step change. Moreover, we demonstrated an oscillatory behavior of normal and radial stress in both space and time domains. The stress pulse duration and intensity change with V_0 and depending on V_0 may propagate across the interface. This behavior supports the recent hydrodynamic plasticity model, which serves as an alternative to adiabatic shear instability. Finally, the potential of cold spray to produce titanium silicide for electronic industry is demonstrated.

SUPPLEMENTARY MATERIAL

See the supplementary material for the force field parameters compatible with LAMMPS, extra details on the calculation of splat diameter, and supporting figures for different orientations of the Si substrate and trajectory of atoms upon deformation.

AUTHOR DECLARATIONS

Conflict of Interest

The authors have no conflicts to disclose.

Author Contributions

Mahyar Ghasemi: Data curation (equal); Investigation (equal); Project administration (equal); Software (equal); Visualization (equal); Writing – original draft (equal). **Alireza Seifi:** Formal analysis (supporting); Investigation (supporting); Project administration (supporting); Software (supporting); Writing – original draft (supporting). **Movaffaq Kateb:** Conceptualization (equal); Methodology (equal); Resources (equal); Supervision (equal); Writing – review & editing (equal). **Jon Tomas Gudmundsson:** Conceptualization (supporting); Formal analysis (equal); Validation (equal); Writing – review & editing (equal). **Pascal Brault:** Formal analysis (supporting); Methodology (supporting); Supervision (supporting); Validation (supporting); Writing – review & editing (supporting). **Pirooz Marashi:** Conceptualization (supporting); Resources (supporting); Supervision (supporting); Validation (supporting); Writing – review & editing (supporting).

DATA AVAILABILITY

The data that support the findings of this study are available from the corresponding author upon reasonable request.

REFERENCES

[1]H. Assadi, F. Gärtner, T. Stoltenhoff, and H. Kreye, Acta Mater. **51**, 4379 (2003).
[2]M. A. Adaan-Nyiak and A. A. Tiamiyu, J. Mater. Res. **38**, 69 (2023).
[3]H. Herman, S. Sampath, and R. McCune, MRS Bull. **25**, 17 (2000).
[4]M. Hassani-Gangaraj, D. Veysset, K. A. Nelson, and C. A. Schuh, Scr. Mater. **145**, 9 (2018).
[5]S. Rahmati and A. Ghaei, J. Therm. Spray Technol. **23**, 530 (2014).
[6]A. Fardan, C. C. Berndt, and R. Ahmed, Surf. Coat. Technol. **409**, 126835 (2021).
[7]H. Jami and A. Jabbarzadeh, Appl. Surf. Sci. **489**, 446 (2019).
[8]H. Jami and A. Jabbarzadeh, Appl. Surf. Sci. **542**, 148567 (2021).
[9]E. Samuel, J.-G. Lee, B. Joshi, T.-G. Kim, M.-W. Kim, I. W. Seong, W. Y. Yoon, and S. S. Yoon, J. Alloys Compd. **715**, 161 (2017).
[10]Z. Wang, X. Chen, Y. Gong, B. Zhang, and H. Li, Surf. Coat. Technol. **325**, 52 (2017).
[11]S. An, B. Joshi, A. L. Yarin, M. T. Swihart, and S. S. Yoon, Adv. Mater. **32**, 1905028 (2020).
[12]C. Park, E. Samuel, B. Joshi, T. Kim, A. Aldalbahi, M. El-Newehy, W. Y. Yoon, and S. S. Yoon, Chem. Eng. J. **395**, 125018 (2020).
[13]E. Watanabe, H. Kura, T. Ogawa, Y. Ichikawa, and K. Ogawa, J. Therm. Spray Technol. **32**, 226 (2023).
[14]M. Kateb and K. Dehghani, Int. J. Mod. Phys.: Conf. Ser. **5**, 410 (2012).
[15]M. Kateb, M. Azadeh, P. Marashi, and S. Ingvarsson, J. Nanopart. Res. **20**, 251 (2018).
[16]M. Azadeh, M. Kateb, and P. Marashi, Comput. Mater. Sci. **170**, 109187 (2019).
[17]M. Kateb, IOP SciNotes **1**, 034801 (2020).
[18]H. Gao, L. Zhao, D. Zeng, and L. Gao, "Molecular dynamics simulation of Au cluster depositing on Au surface in cold gas spray," in *Proceedings of the 2007 First International Conference on Integration and Commercialization of Micro and Nanosystems*, Sanya, Hainan, China, 10–13 January 2007 (ASME, New York, 2007), pp. 195–202.
[19]B. Daneshian and H. Assadi, J. Therm. Spray Technol. **23**, 541 (2014).
[20]A. Joshi and S. James, J. Manuf. Process. **33**, 136 (2018).
[21]S. James and K. Shah, Procedia Manuf. **48**, 776 (2020).
[22]S. Rahmati, A. Zúñiga, B. Jodoin, and R. Veiga, Comput. Mater. Sci. **171**, 109219 (2020).
[23]S. Suresh, S.-W. Lee, M. Aindow, H. D. Brody, V. K. Champagne, and A. M. Dongare, Acta Mater. **182**, 197 (2020).
[24]L. Pereira, S. Rahmati, A. Zúñiga, B. Jodoin, and R. Veiga, Comput. Mater. Sci. **186**, 110045 (2021).
[25]M. Kateb, H. Hajihoseini, J. T. Gudmundsson, and S. Ingvarsson, J. Vac. Sci. Technol. A **37**, 031306 (2019).
[26]M. Kateb, J. T. Gudmundsson, and S. Ingvarsson, J. Vac. Sci. Technol. A **38**, 043006 (2020).
[27]M. Kateb, J. T. Gudmundsson, P. Brault, A. Manolescu, and S. Ingvarsson, Surf. Coat. Technol. **426**, 127726 (2021).
[28]S. Goel, N. H. Faisal, V. Ratia, A. Agrawal, and A. Stukowski, Comput. Mater. Sci. **84**, 163 (2014).
[29]D. Gilmore, R. Dykhuizen, R. Neiser, M. Smith, and T. Roemer, J. Therm. Spray Technol. **8**, 576 (1999).
[30]T. Schmidt, F. Gärtner, H. Assadi, and H. Kreye, Acta Mater. **54**, 729 (2006).
[31]A. Moridi, S. M. Hassani-Gangaraj, M. Guagliano, and M. Dao, Surf. Eng. **30**, 369 (2014).
[32]M. P. Allen and D. J. Tildesley, *Computer Simulation of Liquids* (Oxford University, Oxford, 1987).
[33]S. Plimpton, J. Comput. Phys. **117**, 1 (1995).
[34]S. J. Plimpton and A. P. Thompson, MRS Bull. **37**, 513 (2012).
[35]LAMMPS Website, http://lammps.sandia.gov/ (accessed 29 October 2020).
[36]J. Tersoff, Phys. Rev. B **37**, 6991 (1988).
[37]G. Plummer and G. J. Tucker, Phys. Rev. B **100**, 214114 (2019).
[38]L. Verlet, Phys. Rev. **159**, 98 (1967).
[39]T. Schneider and E. Stoll, Phys. Rev. B **17**, 1302 (1978).
[40]N. Ashcroft and D. C. Langreth, Phys. Rev. **156**, 685 (1967).
[41]P. M. Larsen, S. Schmidt, and J. Schiøtz, Model. Simul. Mater. Sci. Eng. **24**, 055007 (2016).
[42]A. Stukowski, Model. Simul. Mater. Sci. Eng. **18**, 015012 (2009).
[43]Ovito Website, http://ovito.org/, version 3.0.0-dev794.
[44]T. J. Colla, R. Aderjan, R. Kissel, and H. M. Urbassek, Phys. Rev. B **62**, 8487 (2000).
[45]C. L. Cleveland and U. Landman, Science **257**, 355 (1992).
[46]M. Hassani-Gangaraj, D. Veysset, V. K. Champagne, K. A. Nelson, and C. A. Schuh, Acta Mater. **158**, 430 (2018).
[47]I. Dowding, M. Hassani, Y. Sun, D. Veysset, K. A. Nelson, and C. A. Schuh, Acta Mater. **194**, 40 (2020).
[48]P. C. King and M. Jahedi, Appl. Surf. Sci. **256**, 1735 (2010).
[49]Y. Liao, *Practical Electron Microscopy and Database*, 2nd ed. (2006), pp. 150, see https://www.globalsino.com/EM/.
[50]R. W. Mann, L. A. Clevenger, and Q. Z. Hong, J. Appl. Phys. **73**, 3566 (1993).
[51]S. Xiong, W. Qi, B. Huang, M. Wang, and Y. Li, Mater. Chem. Phys. **120**, 446 (2010).
[52]H. Assadi, F. Gärtner, T. Klassen, and H. Kreye, Scr. Mater. **162**, 512 (2019).
[53]M. Hassani-Gangaraj, D. Veysset, V. K. Champagne, K. A. Nelson, and C. A. Schuh, Scr. Mater. **162**, 515 (2019).
[54]B. Daneshian, F. Gaertner, H. Assadi, D. Hoeche, W. Weber, and T. Klassen, J. Therm. Spray Technol. **30**, 503 (2021).